

# Multi-view Hybrid Graph Convolutional Network for Volume-to-mesh Reconstruction in Cardiovascular MRI

Nicolás Gaggion<sup>a</sup>, Benjamin A. Matheson<sup>b</sup>, Yan Xia<sup>b</sup>, Rodrigo Bonazzola<sup>b</sup>, Nishant Ravikumar<sup>b</sup>, Zeike A. Taylor<sup>b</sup>, Diego H. Milone<sup>a</sup>, Alejandro F. Frangi<sup>c,d,e,f</sup>, Enzo Ferrante<sup>a,\*</sup>

<sup>a</sup>*Institute for Signals, Systems, and Computational Intelligence, sinc(i) CONICET-UNL, Santa Fe, Argentina*

<sup>b</sup>*Centre for Computational Imaging and Simulation Technologies in Biomedicine (CISTIB), School of Computing, University of Leeds, Leeds, UK*

<sup>c</sup>*Christabel Pankhurst Institute, Division of Informatics, Imaging, and Data Sciences, School of Health Sciences, The University of Manchester, Manchester, UK*

<sup>d</sup>*Department of Computer Science, School of Engineering, The University of Manchester, Manchester, UK*

<sup>e</sup>*Medical Imaging Research Centre (MIRC), Department of Cardiovascular Sciences, KU Leuven, Leuven, Belgium*

<sup>f</sup>*Alan Turing Institute, London, UK*

arXiv:2311.13706v2 [eess.IV] 13 Aug 2024

## Abstract

Cardiovascular magnetic resonance imaging is emerging as a crucial tool to examine cardiac morphology and function. Essential to this endeavour are anatomical 3D surface and volumetric meshes derived from CMR images, which facilitate computational anatomy studies, biomarker discovery, and in-silico simulations. However, conventional surface mesh generation methods, such as active shape models and multi-atlas segmentation, are highly time-consuming and require complex processing pipelines to generate simulation-ready 3D meshes. In response, we introduce HybridVNet, a novel architecture for direct image-to-mesh extraction seamlessly integrating standard convolutional neural networks with graph convolutions, which we prove can efficiently handle surface and volumetric meshes by encoding them as graph structures. To further enhance accuracy, we propose a multiview HybridVNet architecture which processes both long axis and short axis CMR, showing that it can increase the performance of cardiac MR mesh generation. Our model combines traditional convolutional networks with variational graph generative models, deep supervision and mesh-specific regularisation. Experiments on a comprehensive dataset from the UK Biobank confirm the potential of HybridVNet to significantly advance cardiac imaging and computational cardiology by efficiently generating high-fidelity and simulation ready meshes from CMR images.

**Keywords:** Cardiac Imaging, Geometric Deep Learning, Hybrid Graph Convolutional Neural Network, Volume-to-Mesh

## 1. Introduction

Cardiovascular magnetic resonance (CMR) imaging has become an indispensable tool in the diagnosis, treatment planning, and management of cardiovascular diseases. A critical component of advanced cardiac imaging is the extraction of accurate 3D meshes from CMR images. These meshes serve as the foundation for various applications, including computational simulations [1], biomarker discovery [2], and analysis of heart deformation and dynamics [3].

Despite its importance, cardiac mesh extraction remains a challenging task. Traditional methods, such as active shape models [4] and multi-atlas segmentation [5], often require extensive computational resources and can be time-consuming. The inherent variability in heart shapes, sizes, and pathologies further complicates the extraction process, necessitating robust and adaptable methods.

Traditional mesh generation pipelines are complex, involving multiple steps and often requiring manual interventions. Figure 1 and Table 1 illustrate this complexity, comparing different mesh generation approaches and highlighting the numerous

steps, algorithms, and manual interventions typically required in common pipelines.

A particular challenge lies in transitioning from 2D image slices to a cohesive 3D representation, especially when modeling tetrahedral meshes. Current methodologies often require intricate post-processing steps to refine the meshes and make them suitable for simulations [1, 6]. These additional steps can introduce errors and prolong the overall processing time.

Automatic methods for mesh extraction typically involve a concatenation of several stages, including voxel-level segmentation, surface mesh extraction, and volumetric mesh generation [1, 6]. However, voxel-level segmentation techniques, such as U-Net [7] or V-Net [8], are prone to introducing errors due to the local support of convolutional models, potentially resulting in unrealistic masks with holes or spurious segmentations [9]. Alternative approaches based on deforming initial templates have been proposed. These methods estimate displacements of mesh nodes [10, 11] or directly deform the space surrounding a simulation-ready whole heart template [12]. However, the accuracy of these approaches is limited by the quality of the estimated deformations.

Recent work has explored end-to-end neural networks to estimate parameterized shapes directly from images [13, 14].

\*Corresponding author: eferrante@sinc.unl.edu.ar

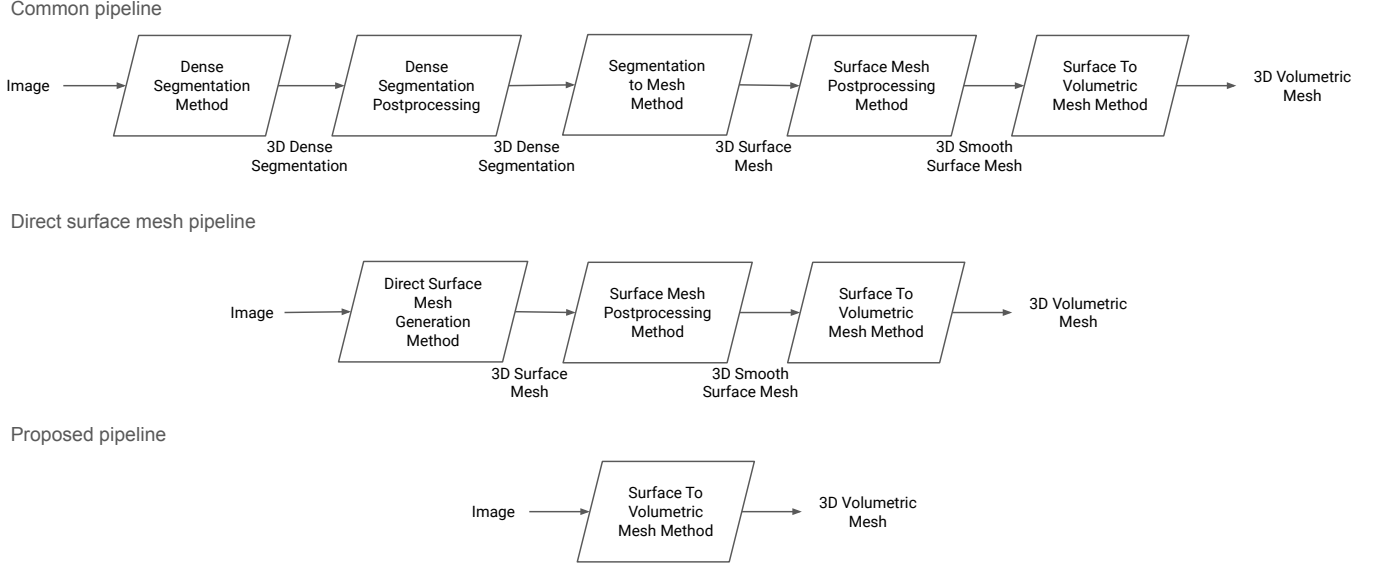


Figure 1: Mesh generation pipelines

These methods use convolutional neural networks to infer the parameters of a Principal Component Analysis (PCA) shape model. While PCA-based models are useful for mesh extraction from volumetric images, their expressiveness is inherently limited by the linearity of PCA.

To address these challenges, we introduce HybridVNet, a novel architecture for generating high-quality surface and volumetric meshes directly from CMR imaging. Our method produces meshes that are immediately suitable for computational models, addressing the limitations of traditional pipelines. By providing an end-to-end solution, HybridVNet eliminates the need for multiple processing steps and manual interventions, streamlining the mesh generation process. It combines standard 3D convolutions for volumetric image encoding with a decoder based on spectral graph convolutions for cardiac mesh generation. This approach enhances the expressiveness of parametric shapes by leveraging a graph-convolutional decoder capable of handling both surface and volumetric meshes.

**Contributions:** Our primary contributions encompass the development of HybridVNet, a multiview volumetric hybrid graph convolutional model capable of seamlessly integrating multiple CMR views within a jointly learned latent space, directly producing meshes from images. Our model exhibits versatility in creating both cardiac surface and tetrahedral meshes, making it suitable for finite element simulations. We explore classic regularization techniques for surface meshes and introduce a novel differentiable regularization term specifically tailored for tetrahedral meshes, markedly enhancing element quality. Notably, while previous works often relied on cropped regions of volumetric images, our model demonstrates exceptional performance in both cropped areas and complete images, showcasing its robustness and adaptability. The performance of HybridVNet is evaluated using the UK Biobank CMR dataset [15], providing a comprehensive assessment in the context of cardiac imaging.

## 2. Volume-to-Mesh extraction in cardiovascular MR

This section details the reference data and mesh generation process used in our study.

### 2.1. Reference CMR meshes and images

The foundation of our study is a reference cohort of 3D surface meshes introduced by Xia et al. (2022) [14]. These meshes were created through a process of registering a high-resolution atlas of the human heart [16] to manually delineated 2D contours at end-diastole (ED) and end-systole (ES) - the points of maximum and minimum ventricular volume in the cardiac cycle, respectively.

The atlas used in this process comprises a mesh that includes six distinct cardiac structures: the left ventricle (LV), right ventricle (RV), left atrium (LA), right atrium (RA), and the ascending aorta. The selection criteria for subjects chosen for manual segmentation and the methodology followed are detailed in Petersen et al. (2017) [17].

A key characteristic of this cohort is that each final ground-truth mesh maintains the same number of nodes and set of faces, resulting in an identical adjacency matrix across all meshes. This consistency is a direct result of the atlas registration process and is particularly advantageous for our graph-based approach, as it allows for uniform processing across all samples. More details about the image and surface mesh dataset are provided in Section 3.1.

### Volumetric mesh dataset generation

We derived volumetric mesh ground-truth annotations from the surface meshes. We used the one-to-one correspondence between surface nodes to register a volumetric atlas to the cardiac surface mesh dataset. The Simpleware software (Version Medical T-2022.03, Synopsys Inc., Mountain View, USA) [18] was used to construct the volumetric atlas mesh. We imported heart

Mesh generation	Process Step	Algorithms involved	Hyper-parameters	Comments
Common pipeline	Segmentation from an 3D image set with dense coverage	Convolutional neural networks, multi-atlas segmentation	CNN architecture selection, neural network training hyperparameters, number of atlases and atlas selection	Explicitly limited by voxel-size and by the rectangular shape of each voxel
	Postprocessing of densely-covering segmentation masks	Artifact removal, smoothing, resampling, hole filling	Size of the artifacts to remove, kernel sizes for smoothing, interpolation method, manual hole filling	Semi automatic procedure, open problem of generating anatomically plausible segmentations
	Generation of surface mesh from segmentation masks	Marching cubes, marching tetrahedra	Grid resolution, isovalue, interpolation method	Grid dependency, staircase effect, limited handling of noise, triangle quality
	Postprocessing surface meshes	Laplacian smoothing, mesh decimation, hole filling, normal smoothing, topological cleaning, edge smoothing	Smoothing factor and iterations, target vertex count, maximum hole size, hole filling method, normal computation method, cleaning methods	Manual intervention required
	Volumetric mesh generation from surface meshes	Delaunay tetrahedralization, quality control, mesh optimization	Tetrahedralization algorithm parameters, surface mesh constraints, boundary preservation thresholds, quality metric selection and threshold, smoothing parameters and optimization objectives	Slow and with manual intervention required
Surface mesh pipeline	Surface mesh extraction directly from 3D images	Convolutional neural networks mixed with point-distribution models	CNN architecture, point distribution model selection, neural network training hyperparameters	Can incorporate anatomical information in the PDM model and generate meshes with no topological artifacts
	Mesh postprocessing	Laplacian smoothing, normal smoothing, edge smoothing	Smoothing factor and iterations, normal computation method	Manual intervention may be required
	Generation of volumetric meshes from surface meshes	Delaunay tetrahedralization, quality control, mesh optimization	Tetrahedralization algorithm parameters, surface mesh constraints, boundary preservation thresholds, quality metric selection and threshold, smoothing parameters and optimization objectives	Slow and with manual intervention required
Proposed volumetric mesh pipeline	Extraction of surface or volumetric meshes directly from raw images	<b>Hybrid graph convolutional neural networks (proposed)</b>	CNN encoder and decoder architectures, neural network training hyperparameters	Incorporates topological information via the adjacency matrix, learns anatomical embeddings in the hybrid network bottleneck, and direct specification of mesh quality via regularization terms at training time.

Table 1: Comparison of Mesh Generation Pipelines

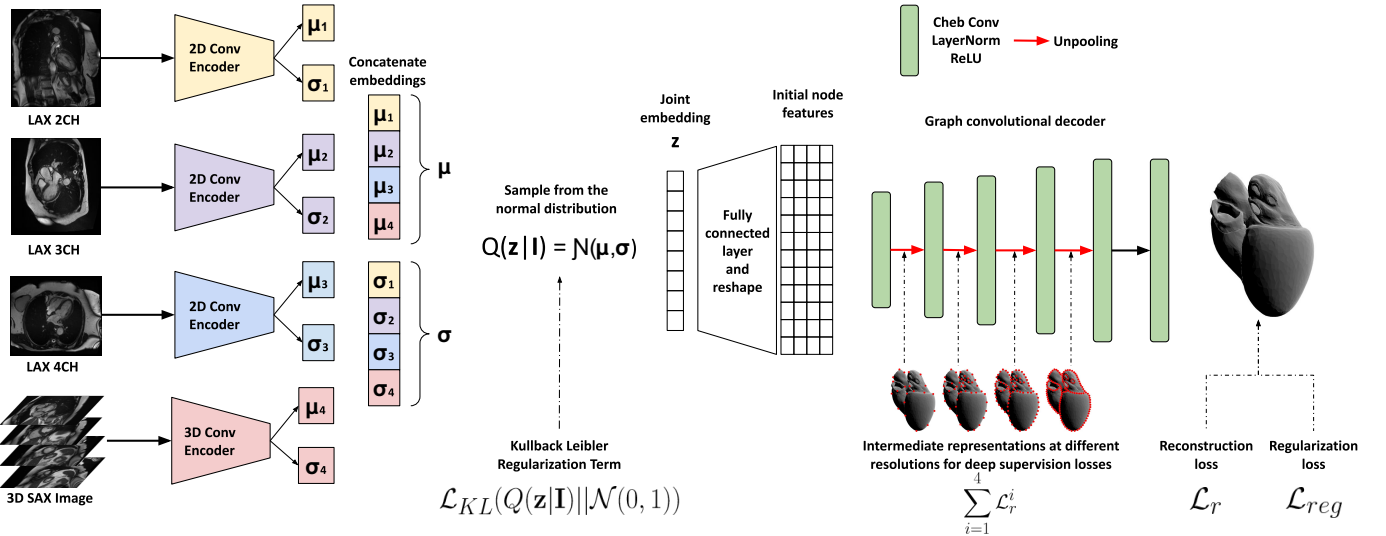


Figure 2: **Multiview HybridVNet model architecture:** The proposed model uses a variational encoder-decoder architecture to generate a graph representation of a desired organ from multiview input images. The encoder consists of independent branches for each input view, concatenated to obtain a joint latent space. The latent code is then passed through a fully connected layer and reshaped to obtain the initial node features for the graph convolutional decoder. This decoder uses the initial node features to generate a final graph representation of the organ.

structures from the human heart atlas [16] as individual closed surface meshes of triangular elements. Then, we populated the hollow surface meshes with tetrahedral elements, setting the elements at the interfaces between different cardiac structures to share nodes. This resulted in a mesh of 408,764 elements. We registered the volumetric atlas on the entire surface dataset using mesh-to-mesh thin plate spline warping, using the Vedo library [19].

## 2.2. HybridVNet formulation

As shown in Figure 2, our HybridVNet model receives multiple CMR views as input: the short-axis view (SAX), which is a 3D cross-sectional view of the heart acquired perpendicular to the long axis, and three different 2D long-axis views (LAX), for two, three and four chambers of the heart (LAX 2CH, LAX 3CH and LAX 4CH, respectively), providing 2D cross-sectional views acquired parallel to the long axis. Given these four images (one volumetric and three 2D), we aim to generate a (surface or tetrahedral) mesh representing the structures of interest.

Consider a dataset  $\mathcal{D} = \{(\mathbf{I}, \mathbf{G})_n\}_{0 < n \leq N}$ , composed of  $N$  samples of multi-view CMR images  $\mathbf{I} = (\mathbf{I}^{\text{LAX 2CH}}, \mathbf{I}^{\text{LAX 3CH}}, \mathbf{I}^{\text{LAX 4CH}}, \mathbf{I}^{\text{SAX}})$ , and their associated cardiac meshes as graphs  $\mathbf{G} = \langle V, \mathbf{A}, \mathbf{X} \rangle$ , where  $V$  is the set of  $M$  nodes or vertices ( $|V| = M$ ),  $\mathbf{A} \in \{0, 1\}^{M \times M}$  is the adjacency matrix indicating the connectivity between pairs of nodes ( $a_{ij} = 1$  indicates an edge connecting vertices  $i$  and  $j$ , and  $a_{ij} = 0$  otherwise), and  $\mathbf{X} \in \mathbb{R}^{M \times s}$  is a function (represented as a matrix) assigning a feature vector to every node. It assigns a 3-dimensional spatial coordinate (the mesh vertex position,  $s = 3$ ). Since our dataset includes meshes with the same number of nodes and the same connectivity by construction, we can use spectral graph convolutions to decode meshes from a latent space [20, 2].

The proposed model consists of a hybrid variational encoder-decoder architecture with multiple inputs. An image convolutional encoder, learns a latent representation of the input images, and a spectral graph convolutional decoder generates a graph representation of the organ. Since our input consists of four images with varying shapes and views, we use a multiview encoder to handle it. To this end, independent encoder branches are defined for each image view, and a joint latent space is constructed by concatenating their outputs. For all types of LAX images, we use 2D convolutional encoders,  $f_e^{\text{LAX 2CH}}$ ,  $f_e^{\text{LAX 3CH}}$  and  $f_e^{\text{LAX 4CH}}$ , with residual convolutions [21]. For the 3D SAX image, we use a 3D convolutional encoder,  $f_e^{\text{SAX}}$ , consisting of 3D residual blocks interleaved by max-pooling operations.

Consequently, our model uses a variational encoder-decoder architecture to generate a graph representation of a desired organ from multiview input images. The encoder maps the input to a lower-dimensional embedding which represents the parameters of a latent distribution,  $\mathbf{z} = f_e^I(\mathbf{I}^{\text{LAX 2CH}}, \mathbf{I}^{\text{LAX 3CH}}, \mathbf{I}^{\text{LAX 4CH}}, \mathbf{I}^{\text{SAX}})$ . This latent distribution is then sampled using the reparametrisation trick [22], passed through a fully connected layer, and reshaped to obtain initial node features for the graph convolutional decoder,  $f_d^G$ . Following the variational autoencoder formulation, the latent code is

assumed to be sampled from a multivariate Gaussian posterior,  $Q(\mathbf{z}|\mathbf{I}) = \mathcal{N}(\boldsymbol{\mu}, \text{diag}(\boldsymbol{\sigma}))$ . The distribution is parameterised by the concatenation of outputs from the joint multiview encoder,  $(\boldsymbol{\mu}, \boldsymbol{\sigma}) = f_e^I(\mathbf{I})$ . Given a sample of the latent code,  $\mathbf{z}$ , the graph representation of the organ can be obtained through the decoder  $f_d^G(\mathbf{z})$ .

The model is trained by minimising a loss function defined as

$$\mathcal{L} = \mathcal{L}_r(f_d(f_e(\mathbf{I})), \mathbf{G}) + \lambda_{KL} \mathcal{L}_{KL}(Q(\mathbf{z}|\mathbf{I})\|\mathcal{N}(0, 1)), \quad (1)$$

where the first term is the reconstruction loss based on the mean squared error (MSE) of the vertex positions, the second term imposes a unit Gaussian prior  $\mathcal{N}(0, 1)$  for the latent posteriors via the KL divergence loss ( $\mathcal{L}_{KL}$ ) and  $\lambda_{KL}$  is a weighting factor.

### Deeply-supervised spectral graph decoder

To generate the graph representation of the target organ, we employed a decoder constructed using spectral graph convolutional neural networks (GCNN). Spectral convolutions are based on the eigendecomposition of the graph Laplacian matrix. In this context, we adopt the spectral convolutions introduced by Defferrard et al. (2016) [23], which constrain the filters to polynomial filters. This constraint arises from the observation that polynomial filters exhibit strict localisation in the vertex domain, consequently reducing the computational complexity of the convolutional operation. For an in-depth understanding of spectral convolutions, please refer to [23].

A spectral convolutional layer operates as standard convolutions applied to images and feature maps. It takes an input feature matrix  $\mathbf{X}^\ell$  and produces filtered versions  $\mathbf{X}^{\ell+1}$  as output. Our spectral decoder architecture comprises five graph-convolutional layers, each complemented by ReLU nonlinearities with previous Layer Normalisation [24]. These layers are strategically interleaved with four fixed graph unpooling layers, allowing the network to learn representations at multiple resolutions.

We implement the technique outlined by Ranjan et al. (2018) [20] to obtain these multiple resolutions to construct pairs of pooling and unpooling layers. The process begins by estimating the pooling matrix, achieved through an iterative contraction of vertex pairs while maintaining precise surface error approximations using quadric matrices into the atlas surface mesh. Simultaneously, the unpooling matrix is derived to enable the reversal of the pooling transformation. This process is repeated four times (in the previously pooled version of the atlas), resulting in four sets of pooling and unpooling layers, each reducing and increasing the number of nodes by a factor of two, respectively. Importantly, these pooling and unpooling matrices remain fixed during training, as they are estimated only once for the atlas surface mesh.

To increase our model’s performance, we apply the concept of deep supervision [25], which involves supervising the network at various resolution levels. During training, we utilise the estimated pooling operation to obtain down-sampled versions of the ground-truth meshes, enabling us to minimise the

reconstruction error at each resolution level. Ultimately, we employ a final graph-convolutional layer, without bias and identity activation function, to predict the final vertex positions.

The incorporation of deep supervision terms leads to the following loss function:

$$\mathcal{L} = \mathcal{L}_r + \lambda_{KL}\mathcal{L}_{KL} + \lambda_{DS} \sum_{i=1}^4 \mathcal{L}_r^i, \quad (2)$$

where  $\mathcal{L}_{KL}$  is the previously defined KL term,  $\lambda_{DS}$  is a weighting factor, and the index  $i$  indicates the resolution level of the graph.

### Mesh regularisation loss functions

To ensure smooth meshes, state-of-the-art approaches to surface mesh generation often use regularisers such as normal regularisation, edge length regularisation, and Laplacian smoothing ( $\mathcal{L}_{lap}$ ), as introduced in [26], which we also incorporate. However, these existing metrics were initially designed for triangular surface meshes and, therefore, do not consider the structure of tetrahedral elements in a volumetric mesh [11]. We propose a new regularisation loss function designed to generate tetrahedral volumetric meshes to address this limitation directly. We introduce our new *tetrahedral element regularisation* loss,

$$\mathcal{L}_{ter} = \frac{1}{N_t} \sum_{i=1}^{N_t} \frac{1}{6} \sum_{j=1}^6 \left( \|\mathbf{e}_j^i\|_2 - \frac{1}{6} \left( \sum_{k=1}^6 \|\mathbf{e}_k^i\|_2 \right) \right)^2, \quad (3)$$

where  $N_t$  is the number of tetrahedra,  $i$  represents the  $i^{th}$  tetrahedron and  $\mathbf{e}_j^i$  and  $\mathbf{e}_k^i$  represent the edges of that tetrahedron. This regularization term encourages the formation of well-shaped tetrahedral elements by penalizing large variations in edge lengths within each tetrahedron, promoting more uniform and stable volumetric meshes. Such meshes are crucial for accurate finite element simulations in computational cardiology. The final loss function used to train the model is:

$$\mathcal{L} = \mathcal{L}_r + \lambda_{KL}\mathcal{L}_{KL} + \lambda_{DS} \sum_{i=1}^4 \mathcal{L}_r^i + \lambda_{reg}\mathcal{L}_{reg}, \quad (4)$$

where  $\mathcal{L}_{reg}$  can be any of the regularisation losses mentioned above:  $\mathcal{L}_{lap}$  for the surface case or  $\mathcal{L}_{ter}$  for the volumetric case, and  $\lambda_{reg}$  is the corresponding weighting factor.

## 3. Experimental Setup

### 3.1. Data and annotations

Data for this study were collected from the UK Biobank (UKB) under access applications 2,964 and 11,350. The study adhered to the guidelines outlined in the Declaration of Helsinki and received ethical approval from the National Research Ethics Service of the National Health Service on 17 June 2011 (Ref 11/NW/0382) and extended on 10 May 2016 (Ref 16/NW/0274). Informed consent was obtained from all participants. The UKB resource is available for researchers to use for public-interest health-related research. The rationale behind the

UKB imaging study is explained in Petersen et al. (2013) [27], and the CMR acquisition protocol is detailed in Petersen et al. (2015)[15].

We performed our experiments on train/test splits from 4525 UKB subjects. To ensure a fair comparison with previous work and facilitate the reproducibility of our results, we used the same train/test splits as Xia et al. [14], in which 600 subjects were reserved as a separate test split. This allowed us to consistently evaluate and compare the model’s performance with previous studies.

### Image and mesh pre-processing

CMR images were pre-processed by normalising intensities to the range [0, 1]. SAX images had dimensions ranging from (100, 100, 6) to (200, 200, 16) and a voxel spacing of [1.82, 1.82, 10] mm, while LAX images had varying dimensions depending on the associated SAX image. To handle different sizes of SAX images between subjects, we evaluated our model in two settings: (1) *Full image input*, where we padded all SAX images to (210, 210, 16), and (2) *Cut input*, where we followed previous work [28, 14] and cropped SAX images to (100, 100, 16), padding slices as needed. In all cases, the LAX images were zero-padded to have a square shape of size (224, 224).

Inspired by classic object detection approaches, we align the vertex positions of the mesh with their relative position inside the SAX image, which is effective when using graph generative models for landmark detection [29]. We first remove the origin of the SAX image and divide each direction by the corresponding voxel spacing to obtain the positions in the voxel space. For the full-image pipeline, we add the padding applied to the positions and divide by the image size. For the cropped-image pipeline, we subtract the origin of the bounding box and divide it by the image size. With this, we obtain a *relative positional space* for training the models, with a value of (0.5, 0.5, 0.5) indicating a node in the centre of the SAX image. To evaluate the results, we reversed this operation and recovered the original positions in millimetres.

### Data augmentation

All models were trained using online data enhancement, including intensity enhancement, random rotations of the SAX images (between -10 and 10 degrees), and arbitrary scaling on the x and y axes. The LAX images were scaled to match the scaling performed in the associated SAX image using each LAX image’s respective direction vector. We added a step to randomly choose the cropping centre for the cropped model, ensuring that the entire heart is always inside the region. This helps the model avoid dependence on a perfectly centred crop and is an extra data augmentation step.

### 3.2. Model implementation and training details

All models were implemented in Python using the PyTorch framework [30]. The PyTorch Geometric library [31] was used for the spectral graph convolutional neural network (GCNN) layers. Hyperparameters were selected through grid search, with the  $k$  hop neighbourhood parameter [23] set to 6. We

Metrics	MCSI-Net SAX		HybridVNet		MCSI-Net SAX-LAX	MV-HybridVNet	
	Cropped	Full Image	Cropped	Cropped	Full Image	Cropped	
LV Endo	DC $\uparrow$	0.87 (0.05)	0.89 (0.05)	<b>0.90 (0.04)</b>	0.88 (0.05)	0.90 (0.04)	<b>0.91 (0.04)</b>
	HD $\downarrow$	5.13 (1.97)	4.48 (1.32)	<b>4.08 (1.22)</b>	4.74 (1.75)	4.22 (1.22)	<b>3.89 (1.18)</b>
	MCD $\downarrow$	1.93 (0.83)	1.67 (0.55)	<b>1.49 (0.49)</b>	1.86 (0.79)	1.55 (0.51)	<b>1.39 (0.46)</b>
LV Myo	DC $\uparrow$	0.76 (0.09)	0.80 (0.06)	<b>0.83 (0.05)</b>	0.78 (0.08)	0.81 (0.05)	<b>0.84 (0.04)</b>
	HD $\downarrow$	5.31 (1.98)	4.71 (1.36)	<b>4.23 (1.27)</b>	4.75 (1.76)	4.40 (1.26)	<b>3.96 (1.23)</b>
	MCD $\downarrow$	1.97 (0.95)	1.71 (0.56)	<b>1.49 (0.51)</b>	1.86 (0.82)	1.57 (0.52)	<b>1.35 (0.46)</b>
RV Endo	DC $\uparrow$	0.85 (0.06)	0.85 (0.05)	<b>0.86 (0.05)</b>	0.85 (0.06)	0.86 (0.05)	<b>0.87 (0.05)</b>
	HD $\downarrow$	7.11 (2.78)	6.97 (2.31)	<b>6.44 (2.19)</b>	7.06 (2.64)	6.79 (2.23)	<b>6.13 (2.23)</b>
	MCD $\downarrow$	2.34 (0.98)	2.10 (0.64)	<b>1.90 (0.57)</b>	2.27 (0.95)	1.99 (0.59)	<b>1.76 (0.59)</b>

Table 2: Quantitative ventricle segmentation results for surface meshes. An up arrow ( $\uparrow$ ) indicates that higher values are better, while a down arrow ( $\downarrow$ ) indicates that lower values are better.

conducted training for 600 epochs using the Adam optimiser with a learning rate of  $1\text{E} - 4$ . The batch size was set to 4, and the weight decay was applied at  $1\text{E} - 5$ . A KL divergence weight factor of  $\lambda_{KL} = 1\text{E} - 5$  was introduced, and a learning rate decline with a factor of 0.99 occurred after each epoch. The 2D and 3D Convolutional Neural Network (CNN) encoders consisted of six residual blocks [32]. In 2D encoders, the maxpooling layers were interleaved with these blocks. In 3D encoders, max-pooling was applied on the X and Y axes between each residual block, with Z-axis max-pooling at the third layer. After a grid search hyperparameter selection, the latent representations were obtained using fully connected layers in the encoders, with a dimension of 32 for the 3D encoder and 8 for all 2D encoders. GCNN decoders, in both 2D and 3D models, comprised six layers of Chebyshev convolutions with Layer Normalisation [24] and ReLU nonlinearities. Classic surface regularisation losses from the PyTorch3D library [33] were used. These losses included edge length, normal vector, and Laplacian regularisation terms.

Source code is available at [https://github.com/ngaggion/HybridNet\\_3D](https://github.com/ngaggion/HybridNet_3D).

### 3.3. Model comparison

We implemented different single- and multiview variants of the HybridVNet architecture. We also compared our approach with the results obtained by the Multi-Cue Shape Inference Network (MCSI-Net) [14] for the dense segmentation task of the ventricle, which constitutes the state-of-the-art point distribution models in this particular data set. MCSI-Net combines two different networks. The first is a position-inference network that predicts the central coordinates of the mesh and a rotation vector. The second is a shape-inference network that uses CNN layers to infer the parameters of a point distribution model (PDM) based on PCA. This model uses the same SAX and multiple LAX views as ours, but also incorporates patient metadata information into the PDM learning process. On the contrary, our model does not require patient metadata. By comparing our HybridVNet with MCSI-Net, we aim to demonstrate the effectiveness of our approach in generating high-quality cardiac meshes without relying on patient metadata. This comparison allows us to evaluate the performance of our model against a

state-of-the-art method, highlighting the strengths of our graph-based, multi-view approach.

## 4. Results and Discussion

We conducted a comprehensive series of experiments to evaluate the performance of the proposed HybridVNet model alongside the baseline models and their various configurations. These experiments covered surface and tetrahedral volumetric mesh scenarios, including a sensitivity analysis of the proposed regularisation losses. All evaluations were carried out on the same test dataset comprising 600 subjects, as presented in Xia et al. 2022 [14], for the ground truth meshes associated with this dataset.

### 4.1. Surface mesh extraction

To evaluate the quality of cardiac meshes, we used mesh metrics (Table 3) and mask-based metrics (Table 2). First, to enable a direct comparison MCSI-Net, which was evaluated directly on the segmentation masks generated by the model in the SAX image space, we derived dense segmentation masks from the surface meshes. Then, we evaluated classic segmentation metrics such as Dice coefficient, Hausdorff distance, and the average distance between the reference and predicted contours in each slice.

In our initial comparison, we evaluated our HybridVNet against the SAX-only MCSI-Net with full images and cropped versions centred on the structure of interest (Table 2). Remarkably, HybridVNet outperforms SAX MCSI-Net for all metrics and structures. Next, we compare our MV-HybridVNet with the standard MCSI-Net, which also incorporates multiple views and is the current state of the art for this data set. The results demonstrate the superiority of our MV-HybridVNet, as it outperforms the standard MCSI-Net across all segmentation metrics for both the left and right ventricle segmentation tasks.

Our *full image* variant of the model achieves better results compared to the baselines, all while eliminating the need for an additional step to detect the region of interest during the segmentation process. Furthermore, the MV-HybridVNet model on *cropped images* beats the results with significant differences relative to the full image.

Subpart	Metric	Full SAX Image		Cropped SAX Image	
		HybridVNet	MV-HybridVNet	HybridVNet	MV-HybridVNet
Full Mesh	MAE ↓	2.56 (0.62)	<b>2.26 (0.55)</b>	2.43 (0.59)	<b>2.18 (0.54)</b>
	MSE ↓	12.20 (7.11)	<b>9.29 (5.48)</b>	11.27 (6.69)	<b>8.80 (5.31)</b>
	RMSE ↓	3.38 (0.89)	<b>2.95 (0.76)</b>	3.25 (0.86)	<b>2.87 (0.76)</b>
LV	MAE ↓	1.90 (0.57)	<b>1.79 (0.55)</b>	1.75 (0.54)	<b>1.70 (0.54)</b>
	MSE ↓	6.23 (4.28)	<b>5.60 (4.03)</b>	5.35 (3.83)	<b>5.11 (3.67)</b>
	RMSE ↓	2.39 (0.73)	<b>2.26 (0.71)</b>	2.21 (0.70)	<b>2.15 (0.70)</b>
RV	MAE ↓	2.18 (0.64)	<b>2.08 (0.60)</b>	2.00 (0.58)	<b>1.97 (0.59)</b>
	MSE ↓	8.39 (5.64)	<b>7.69 (4.93)</b>	7.12 (4.84)	<b>7.04 (4.72)</b>
	RMSE ↓	2.78 (0.82)	<b>2.66 (0.78)</b>	2.56 (0.76)	<b>2.54 (0.78)</b>
LA	MAE ↓	2.90 (1.00)	<b>2.37 (0.78)</b>	2.84 (0.99)	<b>2.30 (0.77)</b>
	MSE ↓	15.40 (13.73)	<b>10.07 (9.74)</b>	14.88 (13.29)	<b>9.58 (9.24)</b>
	RMSE ↓	3.69 (1.33)	<b>3.00 (1.02)</b>	3.63 (1.31)	<b>2.92 (1.02)</b>
RA	MAE ↓	3.07 (0.96)	<b>2.57 (0.76)</b>	2.98 (0.93)	<b>2.51 (0.80)</b>
	MSE ↓	17.46 (13.65)	<b>12.00 (9.42)</b>	16.67 (13.13)	<b>11.75 (10.16)</b>
	RMSE ↓	3.97 (1.32)	<b>3.30 (1.05)</b>	3.87 (1.30)	<b>3.24 (1.11)</b>
AORTA	MAE ↓	2.66 (0.93)	<b>2.37 (0.84)</b>	2.56 (0.89)	<b>2.34 (0.83)</b>
	MSE ↓	13.17 (11.05)	<b>10.24 (8.71)</b>	12.38 (10.52)	<b>10.04 (8.43)</b>
	RMSE ↓	3.41 (1.23)	<b>3.01 (1.09)</b>	3.31 (1.20)	<b>2.97 (1.09)</b>

Table 3: Quantitative mesh evaluation results for surface meshes. An up arrow (↑) indicates that higher values are better, while a down arrow (↓) indicates that lower values are better.

To account for structures that may not be visible in SAX images and to provide more insight into how the incorporation of long-axis views in our model helps the model learn more details about the complete heart structure, we conducted a thorough evaluation of our proposed models directly on various subparts of the output mesh. Standard mesh evaluation metrics, including vertex mean squared error (MSE), mean average error (MAE) and root mean squared error (RMSE), were calculated in millimetres. Table 3 summarises the results in our models, comparing HybridVNet with its multiview version for *cropped images* and *full images* versions independently. Evaluation was performed at the nodes of the left ventricle (LV), right ventricle (RV), left atrium (LA), right atrium (RA) and aorta.

Comparing the performance of the HybridVNet with and without the inclusion of LAX images, we observed a significant improvement in accuracy for all parts of the mesh. This improvement is particularly pronounced for the left and right atria (LA and RA) and the aorta, which are not fully visible in SAX images. The base HybridVNet model demonstrates the ability to approximate the positions of these structures, with further refinement achieved through the integration of LAX images.

### Surface mesh regularisation effect

In the context of the surface mesh experiment, we performed a comprehensive evaluation of various surface regularisation loss functions to enhance the performance of our HybridVNet model. Specifically, we investigated the efficacy of three distinct regularisation approaches: normal regularisation, edge-length regularisation, and Laplacian smoothing. For more information on these regularisers, see [26].

Notably, while commonly employed in mesh regularisation tasks, normal regularisation, and edge length regularisation did

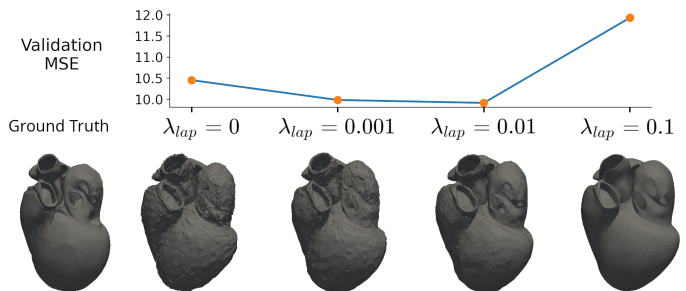


Figure 3: Qualitative analysis of the impact of Laplacian regularisation term on surface mesh smoothness. It demonstrates the influence of adjusting the regularisation parameter on mesh quality. The best quantitative results regarding MSE for the validation split were achieved when  $\lambda_{lap} = 0.01$ .

not yield significant improvements in our model’s performance. This observation aligns with the intuitive understanding that these metrics are better suited for meshes with varying node counts and highly irregular target shapes. This is not the case in our dataset. In contrast, the incorporation of Laplacian smoothing produced notably smoother surface meshes. This can be visually appreciated in Figure 3, which presents a qualitative analysis of the meshes obtained as the regularisation parameter for the Laplacian regularisation loss was increased. Figures clearly illustrate the enhanced smoothness and quality of the meshes as the regularisation strength is adjusted.

To assess the impact of different loss terms during the training process, we refer to Figure 4. This figure provides a comparison of the MSE values throughout both the training and validation phases. Notably, due to the resource-intensive nature of the validation process, we adjusted the intervals when recording loss values, with smaller intervals as more training time elapsed.

Significantly, the red curve in Figure 4 illustrates that the



Table 4: Quantitative results for segmentation metrics in volumetric meshes. ( $\uparrow$ ) indicates that higher results are better, while ( $\downarrow$ ) indicates that lower results are better. Bold results in two columns indicate there are no significant differences between these two.

Metrics		MV-HybridVNet			
		$\lambda_{ter} = 0$	$\lambda_{ter} = 1E-4$	$\lambda_{ter} = 1E-3$	$\lambda_{ter} = 1E-2$
<b>Mesh</b>	MAE $\downarrow$	2.08 (0.63)	2.07 (0.64)	<b>2.04 (0.61)</b>	2.11 (0.61)
	MSE $\downarrow$	8.25 (6.14)	8.22 (6.12)	<b>7.93 (5.63)</b>	8.39 (6.00)
	RMSE $\downarrow$	2.74 (0.88)	2.73 (0.88)	<b>2.69 (0.84)</b>	2.77 (0.84)
<b>LV Endo</b>	DC $\uparrow$	<b>0.90 (0.04)</b>	<b>0.90 (0.04)</b>	0.90 (0.05)	0.88 (0.05)
	HD $\downarrow$	<b>4.36 (1.22)</b>	<b>4.32 (1.24)</b>	4.41 (1.35)	5.21 (1.42)
	MCD $\downarrow$	<b>1.52 (0.46)</b>	<b>1.51 (0.49)</b>	1.58 (0.54)	1.89 (0.62)
<b>LV Myo</b>	DC $\uparrow$	<b>0.78 (0.04)</b>	<b>0.78 (0.04)</b>	0.76 (0.05)	0.74 (0.06)
	HD $\downarrow$	5.27 (1.47)	<b>4.98 (1.40)</b>	5.17 (1.50)	5.30 (1.57)
	MCD $\downarrow$	1.86 (0.61)	<b>1.81 (0.64)</b>	1.95 (0.72)	1.96 (0.77)
<b>RV Endo</b>	DC $\uparrow$	0.85 (0.06)	<b>0.86 (0.05)</b>	0.85 (0.05)	0.85 (0.06)
	HD $\downarrow$	7.22 (2.76)	<b>6.97 (2.54)</b>	7.38 (2.67)	7.55 (2.80)
	MCD $\downarrow$	2.05 (0.64)	<b>2.02 (0.63)</b>	2.09 (0.64)	2.13 (0.69)

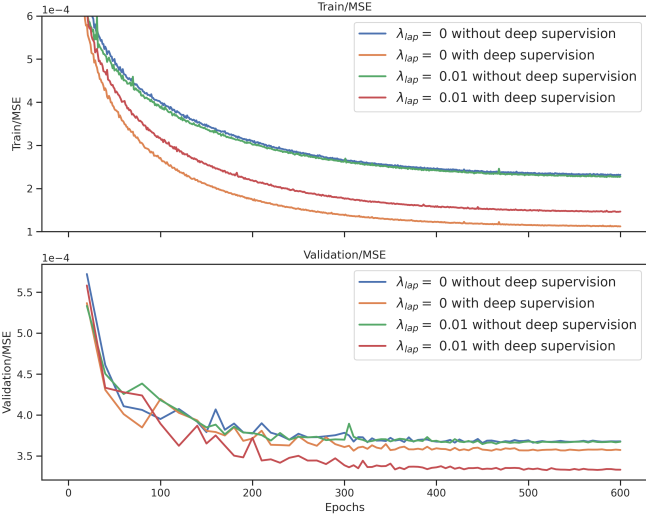


Figure 4: MSE values throughout training and validation for different configurations of hyperparameters, measured in the *relative positional space*. The red curve highlights the significant impact of combining deep supervision and Laplacian regularisation losses on model performance. Smaller intervals were used for loss recording as training progressed.

best performance is achieved when combining both deep supervision and Laplacian regularisation losses. This combination eases the training process and leads to improved model performance. The optimal regularisation strength for Laplacian smoothing, resulting in the best MSE for the entire image and cropped models, was determined to be  $\lambda_{lap} = 0.01$ . This finding was consistent with both qualitative and quantitative evaluations, as over-smoothed meshes appeared when using high values of the regularisation term.

#### 4.2. Towards simulation-ready tetrahedral meshes

Our second experiment focused on the creation of simulation-ready tetrahedral meshes. We evaluated various weighting factors ( $\lambda_{ter}$ ) for the term of regularisation of the tetrahedral element defined in (3), to understand its influence on both the quality of the mesh and the performance of ventricle

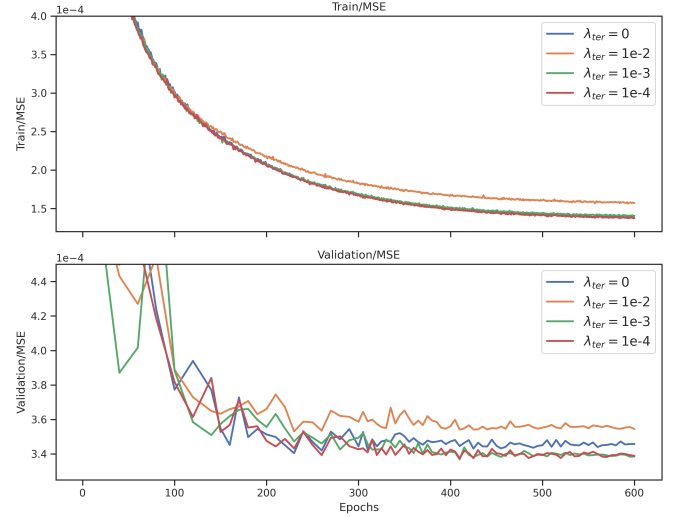


Figure 5: MSE values throughout training and validation for volumetric meshes, exploring different configurations of  $\lambda_{ter}$ , with values measured in the *relative positional space*. Noticeably,  $\lambda_{ter} = 1E-2$  (Yellow) shows a high-performance decay for both train and validation curves. Smaller intervals were used for loss recording as training progressed.

segmentation. Table 4 presents the results, including metrics for mesh quality and ventricle segmentation, in different  $\lambda_{ter}$  values.

Our exploration reveals a nuanced relationship between  $\lambda_{ter}$  and the model’s performance. In particular, the best outcomes emerge for segmentation metrics when  $\lambda_{ter} = 1E-4$ . In this configuration, the results closely resemble the non-regularised model, especially concerning the LV Endo metrics. However, for metrics related to mesh prediction performance, the optimal choice changes slightly, with  $\lambda_{ter} = 1E-3$  yielding the best outcomes. Although this setting leads to a minor drop in ventricle segmentation performance, it significantly reduces the mesh error.

A closer examination of the training dynamics, as illustrated in Figure 5, reinforces the benefits of using small values of  $\lambda_{ter}$ . These values result in improved validation performance without



Table 5: Quantitative results for the quality of elements in volumetric meshes. The values correspond to the scaled Jacobian, and higher values imply a better quality of the tetrahedra.

		Mean	Std	Min	Max	1%	5%	25%	50%	75%
<b>Reference Meshes</b>	Atlas	0.491	0.174	0.092	0.984	0.115	0.194	0.367	0.494	0.617
	Ground Truth	0.355	0.156	-0.207	0.838	0.04	0.103	0.238	0.353	0.47
	Simpleware	0.524	0.185	0.064	0.992	0.128	0.202	0.387	0.535	0.667
<b>MV-HybridGNet3D</b>	$\lambda_{ter} = 0$	0.222	0.225	-0.759	0.876	-0.327	-0.144	0.065	0.219	0.384
	$\lambda_{ter} = 1E-4$	0.229	0.23	-0.771	0.871	-0.337	-0.151	0.068	0.231	0.397
	$\lambda_{ter} = 1E-3$	0.433	0.206	-0.719	0.904	-0.138	0.059	0.307	0.457	0.585
	$\lambda_{ter} = 1E-2$	0.501	0.309	-0.931	0.943	-0.681	-0.298	0.434	0.577	0.688

substantial fluctuations in the training curves. On the contrary, the highest regularisation strength ( $\lambda_{ter} = 1E-2$ ) leads to decreased performance in both training and validation. Note that the impact of the regularisation term on the ventricle segmentation metrics reported is not drastic. However, as demonstrated in Figure 6 and elaborated in the following paragraphs, it substantially increases the quality of tetrahedral elements, a critical consideration for simulations.

We used the widely adopted scaled Jacobian metric to validate the quality of tetrahedral elements. The Jacobian of a tetrahedron is a matrix that describes how the tetrahedron’s shape changes under deformation. The scaled Jacobian is a quantitative measure of regularity and symmetry, falling within the range  $[-1, 1]$  and not affected by scale or units. A high-scaled Jacobian value implies high regularity, low distortion, and therefore high quality [34]. Table 5 provides a comprehensive overview of element quality under different  $\lambda_{ter}$  conditions. The table includes statistics such as the average, standard deviation, minimum, maximum, and various percentiles of the quality of tetrahedron in all test subjects. We compare our approaches with volumetric atlases, ground truth meshes, and a subset of surface meshes converted to volumetric meshes using Simpleware’s ScanIP [18].

Importantly, these findings demonstrate that our regularised models surpass ground-truth elements in terms of quality, beginning from the 25% quartile and onwards, for  $\lambda_{ter} = 1E-3$  and higher. This observation underscores our hypothesis that the regularisation loss significantly enhances the mesh quality. Figure 6 visually summarises this improvement, positioning our method competitively with Simpleware meshes, except for a small number of elements, potentially due to the original low quality of the ground truth.

Overall, our model demonstrates competitive results compared to the conventional approach of directly converting surface to volumetric meshes. Moreover, it addresses a challenge posed by direct conversion, where degenerate triangles can obstruct the creation of volumetric meshes, affecting approximately 10% of cases in our experiments. When comparing the time required for generating a volumetric mesh, Simpleware’s ScanIP procedure consumes approximately 6 minutes on average for each mesh, employing the same configuration as used in the atlas generation procedure. In contrast, our approach requires less time for generating the vertex set of volumetric meshes. When executed on an NVIDIA A100-SXM4 GPU, it accomplishes this task in just 0.04 seconds for each set of CMR

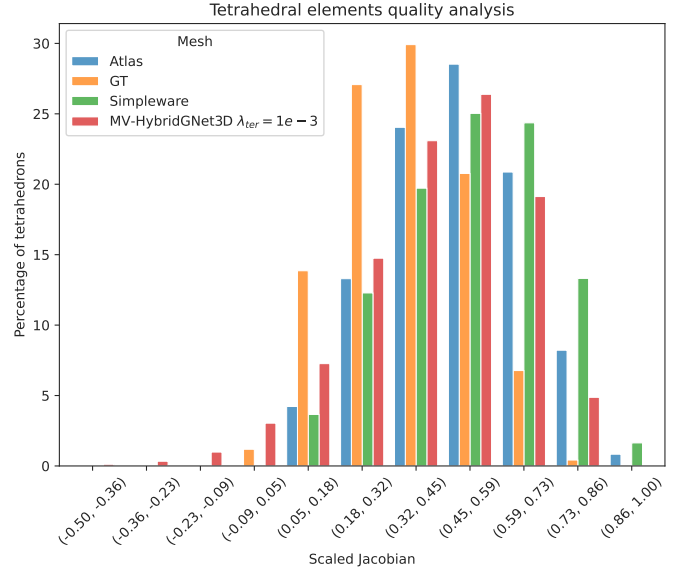


Figure 6: Histogram of tetrahedral mesh quality using scaled Jacobian values. The x-axis represents the scaled Jacobian values, and the y-axis shows the percentage of tetrahedral elements within each range.

images during the forward pass, resulting in a substantial speed improvement. Even in cases where GPU computing is unavailable, when running on an Intel(R) Core(TM) i7-7700 CPU operating at 3.60GHz, the forward pass requires only 5 seconds on average, providing a significant acceleration.

## 5. Conclusions

This study introduces HybridVNet, a novel method for directly generating surface and tetrahedral meshes from images. Our comprehensive experiments and evaluations reveal that HybridVNet significantly enhances mesh accuracy and versatility compared to state-of-the-art point distribution models that depend on linear PCA component decoding. In particular, integrating short- and long-axis views has yielded improved results, capturing finer details of the complete cardiac structure. HybridVNet stands out for its efficiency and speed, substantially reducing vertex set generation time compared to conventional approaches, a precious trait for large-scale processing such as in studies on the UK Biobank. The generic nature of HybridVNet opens doors to broader applications in medical image analysis, with potential extensions to tasks such as cortical surface

reconstruction from brain magnetic resonance images. Future work will direct efforts toward enhancing the element quality of the tetrahedral ground truth used for model training, ensuring more accurate evaluations of our method’s potential for in-silico simulation-based studies.

## Acknowledgments

AFF acknowledges support from the Royal Academy of Engineering under the RAEng Chair in Emerging Technologies (INSILEX CiET1919/19) and the ERC Advanced Grant – UKRI Frontier Research Guarantee (INSILICO EP/Y030494/1). EF acknowledges support from Nvidia for the donation of GPU computing, the Argentinian Agencia Nacional de Promoción de la Investigación, el Desarrollo Tecnológico y la Innovación (PICT PRH 2019-0009), and Universidad Nacional del Litoral (CAID project).

## References

- [1] M. Fedele and A. Quarteroni, “Polygonal surface processing and mesh generation tools for the numerical simulation of the cardiac function,” *International Journal for Numerical Methods in Biomedical Engineering*, vol. 37, no. 4, p. e3435, 2021.
- [2] R. Bonazzola, N. Ravikumar, R. Attar, E. Ferrante, T. Syeda-Mahmood, and A. F. Frangi, “Image-derived phenotype extraction for genetic discovery via unsupervised deep learning in CMR images,” in *MICCAI*. Springer, 2021, pp. 699–708.
- [3] M. Beetz, J. C. Acero, A. Banerjee, I. Eitel, E. Zaccur, T. Lange, T. Stiermaier, R. Evertz, S. J. Backhaus, H. Thiele, A. Bueno-Orovio, P. Lamata, A. Schuster, and V. Grau, “Mesh u-nets for 3d cardiac deformation modeling,” in *Statistical Atlases and Computational Models of the Heart. Regular and CMR Motion Challenge Papers*, O. Camara, E. Puyol-Antón, C. Qin, M. Sermesant, A. Suinesiaputra, S. Wang, and A. Young, Eds. Cham: Springer Nature Switzerland, 2022, pp. 245–257.
- [4] S. Ordas, E. Oubel, R. Leta, F. Carreras, and A. F. Frangi, “A statistical shape model of the heart and its application to model-based segmentation,” in *Medical Imaging 2007: Physiology, Function, and Structure from Medical Images*, vol. 6511. SPIE, 2007, pp. 490–500.
- [5] W. Bai, W. Shi, C. Ledig, and D. Rueckert, “Multi-atlas segmentation with augmented features for cardiac mr images,” *Medical image analysis*, vol. 19, no. 1, pp. 98–109, 2015.
- [6] A. Neic, M. A. Gsell, E. Karabelas, A. J. Prassl, and G. Plank, “Automating image-based mesh generation and manipulation tasks in cardiac modeling workflows using meshtool,” *SoftwareX*, vol. 11, p. 100454, 2020.
- [7] O. Ronneberger, P. Fischer, and T. Brox, “U-net: Convolutional networks for biomedical image segmentation,” in *MICCAI*. Springer, 2015, pp. 234–241.
- [8] F. Milletari, N. Navab, and S.-A. Ahmadi, “V-net: Fully convolutional neural networks for volumetric medical image segmentation,” in *2016 fourth international conference on 3D vision (3DV)*. IEEE, 2016, pp. 565–571.
- [9] A. J. Larrazabal, C. Martínez, B. Glocker, and E. Ferrante, “Post-dae: anatomically plausible segmentation via post-processing with denoising autoencoders,” *IEEE TMI*, 2020.
- [10] E. Puyol-Anton *et al.*, “A multimodal spatiotemporal cardiac motion atlas from mr and ultrasound data,” *Medical image analysis*, vol. 40, pp. 96–110, 2017.
- [11] D. H. Pak, M. Liu, T. Kim, L. Liang, R. McKay, W. Sun, and J. S. Duncan, “Distortion energy for deep learning-based volumetric finite element mesh generation for aortic valves,” in *MICCAI*. Springer International Publishing, 2021, pp. 485–494.
- [12] F. Kong and S. C. Shadden, “Whole heart mesh generation for image-based computational simulations by learning free-from deformations,” in *MICCAI*. Springer, 2021, pp. 550–559.
- [13] K. Tóthová, S. Parisot, M. Lee, E. Puyol-Antón, A. King, M. Pollefeys, and E. Konukoglu, “Probabilistic 3D surface reconstruction from sparse MRI information,” in *International Conference on Medical Image Computing and Computer-Assisted Intervention*. Springer, 2020, pp. 813–823.
- [14] Y. Xia *et al.*, “Automatic 3D+t four-chamber CMR quantification of the UK biobank: integrating imaging and non-imaging data priors at scale,” *Medical Image Analysis*, vol. 80, p. 102498, 2022.
- [15] S. E. Petersen *et al.*, “UK biobank’s cardiovascular magnetic resonance protocol,” *Journal of cardiovascular magnetic resonance*, vol. 18, no. 1, pp. 1–7, 2015.
- [16] C. Rodero *et al.*, “Linking statistical shape models and simulated function in the healthy adult human heart,” *PLOS Computational Biology*, vol. 17, no. 4, pp. 1–28, 04 2021.
- [17] S. E. Petersen, N. Aung, M. M. Sanghvi, F. Zemrak, K. Fung, J. M. Paiva, J. M. Francis, M. Y. Khanji, E. Lukaschuk, A. M. Lee *et al.*, “Reference ranges for cardiac structure and function using cardiovascular magnetic resonance (cmr) in caucasians from the uk biobank population cohort,” *Journal of cardiovascular magnetic resonance*, vol. 19, no. 1, pp. 1–19, 2017.
- [18] Synopsys, “Simpleware,” 2021, <https://www.synopsys.com/simpleware.html>, Last opened on 2023-11-08.
- [19] M. Musy and others., “vedo: 2022.4.1,” Oct. 2022.

- [20] A. Ranjan, T. Bolkart, S. Sanyal, and M. J. Black, “Generating 3D faces using convolutional mesh autoencoders,” in *Proceedings of the European Conference on Computer Vision (ECCV)*, 2018, pp. 704–720.
- [21] K. He, X. Zhang, S. Ren, and J. Sun, “Deep residual learning for image recognition,” in *Proceedings of the IEEE conference on computer vision and pattern recognition*, 2016, pp. 770–778.
- [22] D. P. Kingma and M. Welling, “Auto-encoding variational bayes,” *arXiv preprint arXiv:1312.6114*, 2013.
- [23] M. Defferrard, X. Bresson, and P. Vandergheynst, “Convolutional neural networks on graphs with fast localized spectral filtering,” *arXiv preprint arXiv:1606.09375*, 2016.
- [24] J. L. Ba, J. R. Kiros, and G. E. Hinton, “Layer normalization,” *arXiv preprint arXiv:1607.06450*, 2016.
- [25] C.-Y. Lee, S. Xie, P. Gallagher, Z. Zhang, and Z. Tu, “Deeply-supervised nets,” in *Artificial intelligence and statistics*, 2015, pp. 562–570.
- [26] N. Wang, Y. Zhang, Z. Li, Y. Fu, W. Liu, and Y.-G. Jiang, “Pixel2mesh: Generating 3D mesh models from single rgb images,” in *Proceedings of the European conference on computer vision (ECCV)*, 2018, pp. 52–67.
- [27] S. E. Petersen *et al.*, “Imaging in population science: cardiovascular magnetic resonance in 100,000 participants of UK Biobank - rationale, challenges and approaches,” *Journal of Cardiovascular Magnetic Resonance*, vol. 15, no. 1, p. 46, Dec. 2013.
- [28] R. Attar *et al.*, “Quantitative CMR population imaging on 20,000 subjects of the UK biobank imaging study: Lv/rv quantification pipeline and its evaluation,” *Medical image analysis*, vol. 56, pp. 26–42, 2019.
- [29] N. Gaggion, L. Mansilla, C. Mosquera, D. H. Milone, and E. Ferrante, “Improving anatomical plausibility in medical image segmentation via hybrid graph neural networks: applications to chest x-ray analysis,” *IEEE Transactions on Medical Imaging*, 2022.
- [30] A. Paszke *et al.*, “Pytorch: An imperative style, high-performance deep learning library,” in *Advances in Neural Information Processing Systems*, 2019.
- [31] M. Fey and J. E. Lenssen, “Fast graph representation learning with PyTorch Geometric,” in *ICLR Workshop on Representation Learning on Graphs and Manifolds*, 2019.
- [32] K. He, X. Zhang, S. Ren, and J. Sun, “Deep residual learning for image recognition,” in *2016 IEEE Conference on Computer Vision and Pattern Recognition (CVPR)*, 2016, pp. 770–778.
- [33] N. Ravi *et al.*, “Accelerating 3D deep learning with pytorch3d,” *arXiv:2007.08501*, 2020.
- [34] A. Johnen, C. Geuzaine, T. Toulorge, and J.-F. Remacle, “Efficient computation of the minimum of shape quality measures on curvilinear finite elements,” *Computer-Aided Design*, vol. 103, pp. 24–33, 2018.